

Site-Selective Enhancement of Superconducting Nanowire Single-Photon Detectors via Local Helium Ion Irradiation

Stefan Strothauer,^{1,2,*} Fabian Wietschorke,^{1,3} Lucio Zugliani,^{1,3} Rasmus Flaschmann,^{1,3} Christian Schmid,^{1,3} Stefanie Grotowski,^{1,2} Manuel Müller,^{4,2} Björn Jonas,^{1,3} Matthias Althammer,^{4,2} Rudolf Gross,^{4,2,5} Kai Müller,^{1,3,5} and Jonathan Finley^{1,2,5,†}

¹Walter Schottky Institute, Technical University of Munich, 85748 Garching, Germany

²TUM School of Natural Sciences, Technical University of Munich, 85748 Garching, Germany

³TUM School of Computation, Information and Technology,
Technical University of Munich, 80333 Munich, Germany

⁴Walther-Meißner-Institut, 85748 Garching, Germany

⁵Munich Center for Quantum Science and Technology (MCQST), 80799 Munich, Germany

(Dated: May 23, 2023)

Achieving homogeneous performance metrics between nominally identical pixels is challenging for the operation of arrays of superconducting nanowire single-photon detectors (SNSPDs). Here, we utilize local helium ion irradiation to post-process and tune single-photon detection efficiency, switching current, and critical temperature of individual devices on the same chip. For 12 nm thick highly absorptive SNSPDs, which are barely single-photon sensitive prior to irradiation, we observe an increase of the system detection efficiency from $< 0.05\%$ to $(55.3 \pm 1.1)\%$ following irradiation. Moreover, the internal detection efficiency saturates at a temperature of 4.5 K after irradiation with $1800 \text{ ions nm}^{-2}$. For irradiated 10 nm thick detectors we observe a doubling of the switching current (to 20 μA) compared to 8 nm SNSPDs of similar detection efficiency, increasing the amplitude of detection voltage pulses. Investigations of the scaling of superconducting thin film properties with irradiation up to a fluence of $2600 \text{ ions nm}^{-2}$ revealed an increase of sheet resistance and a decrease of critical temperature towards high fluences. A physical model accounting for defect generation and sputtering during helium ion irradiation is presented and shows good qualitative agreement with experiments.

I. INTRODUCTION

Superconducting Nanowire Single-Photon Detectors (SNSPDs) [1] play a significant role in quantum technologies [2–9] and a wide range of applications requiring general faint light detection [10, 11]. Compared to Single-Photon Avalanche Diodes (SPADs) [12], their superior performance metrics, consisting of high detection efficiency also at long wavelengths [13, 14], low dark count rate [15], and low timing jitter [16] make them ideally suited for demanding applications such as quantum key distribution [2–4], quantum computing [17], or deep space optical communication [7]. Moreover, their waveguide-integrated form is a key component for photonic integrated circuits [18–22].

Since recently, SNSPDs also find application in fields such as astronomy [23], dark matter detection [24], and particle detection [25, 26]. However, these applications typically require large detector arrays or even an SNSPD camera, which to date turns out to be challenging due to the necessary readout and homogeneity within an ensemble of the order of hundreds to thousands of detectors. Recently, row-column multiplexing of a 1024-pixel array [27], and a promising readout architecture based on thermal coupling and time-of-flight measurements [28] were

demonstrated. For such pixel arrays, typically amorphous materials such as MoSi and WSi are used, although SNSPDs based on polycrystalline materials like NbN and NbTiN exhibit higher critical temperatures, larger critical currents, and lower timing jitter. Compared to polycrystalline materials and their spatial inhomogeneities of the superconducting energy gap [29–32], amorphous films attain better homogeneity and the associated higher yield of similarly performing detectors [33–37]. To enable the use of NbN for large pixel arrays, atomic layer deposition and molecular-beam epitaxy of highly homogeneous films have been investigated recently as alternatives to the common deposition of polycrystalline NbN and NbTiN films grown using reactive magnetron sputtering [38–41]. In addition to methods for obtaining better homogeneity during film deposition, a method to tune detector metrics of individual devices after fabrication would also be highly advantageous. Inspired by the recent work of Zhang *et al.* [42], which sparked interest in irradiating SNSPDs with helium (He) ions [43–45], we use a He ion microscope as a post-processing tool to tune detector metrics of individual NbTiN devices fabricated on the same chip. At the same time, we investigate how SNSPD properties such as detection efficiency and switching current depend on the He ion fluence. In addition to detector metrics, we explore the scaling of NbTiN thin film parameters such as sheet resistance and critical temperature with increasing irradiation.

* stefan.strothauer@wsi.tum.de

† finley@wsi.tum.de

II. EXPERIMENTAL

To study the influence of He ion irradiation on the native transport properties of NbTiN thin films and the performance of SNSPDs, we deposited NbTiN films with thicknesses of 8 nm, 10 nm, and 12 nm using DC reactive magnetron sputtering onto Si substrates with a 130 nm thick thermally grown SiO₂ layer. The NbTiN thickness was controlled by measuring the sputtering rate and adjusting the sputtering time correspondingly. Subsequently, we patterned the NbTiN films into cloverleaf structures and SNSPDs using electron beam lithography and reactive ion etching, followed by optical lithography and gold evaporation for contact pad fabrication [46]. The detector design consists of a 100 nm wide wire in a meander form with a fill factor of 50%, and a total active area of 10 $\mu\text{m} \times 10 \mu\text{m}$. The cloverleaf structures were fabricated in order to perform magneto-transport measurements in van-der-Pauw geometry [47, 48] with an active area of 10 $\mu\text{m} \times 10 \mu\text{m}$ and to correlate the results of macroscopic transport with the He ion fluence dependent performance metrics of the corresponding SNSPDs. To ensure the best comparability, cloverleaves (CLs) and SNSPDs were fabricated on the same chip. For this study, they were subsequently irradiated with a He ion microscope (Zeiss Orion Nanofab) with He ion fluences ranging from 0 ions nm⁻² to 2600 ions nm⁻².

The magneto-transport measurements were performed by cooling the samples to 4.2 K before allowing them to slowly heat up to 20 K in external magnetic fields between -0.1 T and 1 T, applied perpendicular to the sample plane. From these measurements, we extract the sheet resistance of the superconducting thin film at 20 K and room temperature, the critical temperature of the superconducting thin film, and the Bogoliubov quasiparticle diffusivity. Also, by measuring the CLs in Hall geometry and performing magnetic field sweeps, followed by a linear fit of the Hall voltage, we determine the Hall coefficient and electron density of the NbTiN films.[49]

Switching current I_{sw} and system detection efficiency (SDE) of the SNSPDs were measured using a cryogenic probe station (Janis) at 4.5 K. To calculate the SDE, we determined the dark count rate (DCR) before we measured the count rate (CR) by homogeneous illumination of the SNSPD with an attenuated 780 nm continuous wave diode laser and polarization parallel to the nanowire. The SDE is then defined as $\text{SDE} = \frac{\text{CR} - \text{DCR}}{\text{PR}}$ with the photon rate PR incident on the cryogenic probe station.

III. RESULTS AND DISCUSSION

In this section, we present the dependence of NbTiN thin film properties and detector metrics on He ion irradiation for film thicknesses of 8 nm, 10 nm, and 12 nm. Provided that the SNSPDs are sensitive to single photons, using larger thicknesses for SNSPDs generally re-

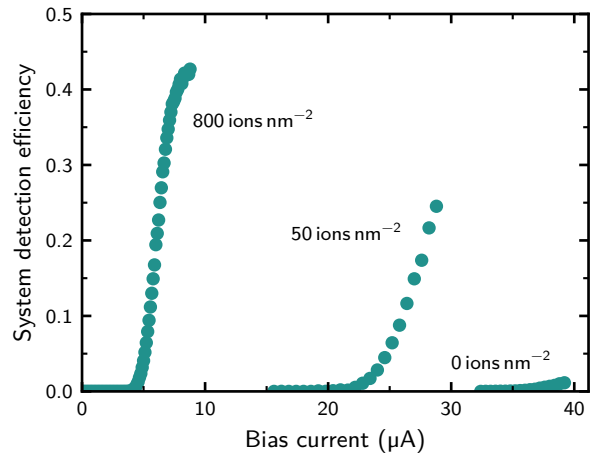


FIG. 1. System detection efficiency vs. bias current of the same 10 nm thick detector for three different He ion fluences. The relative uncertainties of He ion fluence, SDE, and bias current are 5%, 2% and less than 1%, respectively (error bars not shown for clarity). With increasing fluence the efficiency rises up to 43% and shows the beginning of saturating internal detection efficiency, while the switching current decreases. The largest change in SDE and I_{sw} is induced by the first He ions that hit the detector.

sults in stronger optical absorption [50, 51] and therefore enhances their overall system detection efficiency (SDE). Moreover, we aim for a better understanding of how He ion irradiation modifies the transport properties of the NbTiN film and focus on establishing structure-property relationships that link detector thickness, He ion fluence, and detector performance.

A. Performance of He ion irradiated SNSPDs

Figure 1 shows the increase in SDE and the simultaneous decrease of switching current of a representative 10 nm thick device measured before irradiation and after fluences of 50 ions nm⁻² and 800 ions nm⁻². Irradiating the detector with 50 ions nm⁻² already results in an increase in SDE from < 2% to 25%. At a fluence of 800 ions nm⁻² the detector shows the beginning of saturating SDE at 43%, close to the maximum absorption of 53.1% in the detector as determined by finite-difference time-domain (FDTD) simulations (Appendix A). Simultaneously, a decrease in switching current I_{sw} , which is defined as the maximum current the detector can sustain before switching to the normal conducting state, is apparent and ranges from 39.2 μA to 28.8 μA and 8.6 μA after irradiation.

To study the scaling of the switching current with He ion fluence, we irradiated multiple detectors that have thicknesses of 8 nm, 10 nm, and 12 nm using different He ion fluence values. Figure 2 shows the resulting data, revealing a clear trend of decreasing I_{sw} with He ion flu-

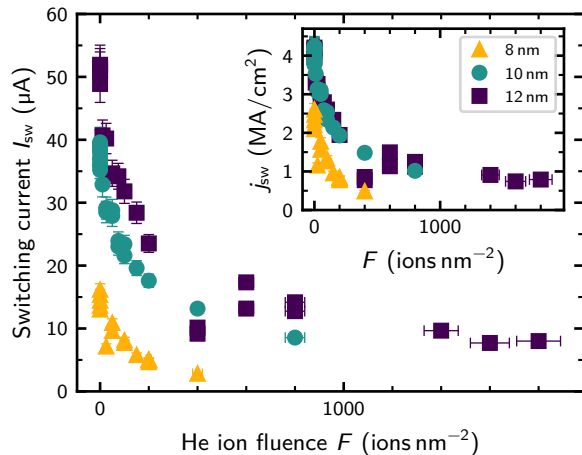


FIG. 2. Switching current vs. He ion fluence for 8 nm, 10 nm, and 12 nm detector thickness, including statistical errors. I_{sw} decreases with the He ion fluence, showing the largest decrease for low fluences. A strong dependence of I_{sw} on the film thickness is apparent throughout the whole fluence range studied. The inset shows the switching current density j_{sw} as calculated from I_{sw} and the wire width and thickness, accounting for an effective thickness reduction due to surface sputtering during He ion irradiation as well as a 1.3 nm thick native NbTiN oxide.

ence. As expected, I_{sw} is higher for thicker devices of the same fluence due to the larger cross-sectional area of thicker nanowires. We explain the scattering of measured switching currents of nominally identical detectors by constrictions that limit I_{sw} to a lower value than non-constricted devices have.[35] Such scatter is particularly visible by the large variation of currents of the non-irradiated devices and the small values of the two 12 nm detectors irradiated with 400 ions nm^{-2} . The inset of Figure 2 shows the switching current density j_{sw} as calculated from I_{sw} and the cross sectional area of the wire, given by the width and the nominal wire thickness presented in Table II. Furthermore, we accounted for an effective reduction of the nominal thickness due to surface sputtering during He ion irradiation as derived in Section III B and for a native NbTiN oxide of 1.3 nm thickness [52]. The switching current density of our non-irradiated NbTiN detectors is comparable to the data Korneeva *et al.* [53] present for 5.8 nm thick NbN devices. Moreover, we observe j_{sw} of the 8 nm film being smaller than for the 10 nm and 12 nm films. We note that for thin and narrow wires, the depairing current density [53, 54] can limit the measurable switching current density and reveals a dependence on the film thickness [55, 56]. Thus, an increased depairing current density for the thicker devices also likely contributes to their higher I_{sw} and j_{sw} .

Similar to I_{sw} , we investigated the scaling of SDE with the He ion fluence. As shown in Figure 3, we observe an increase of SDE with the He ion fluence for all detector

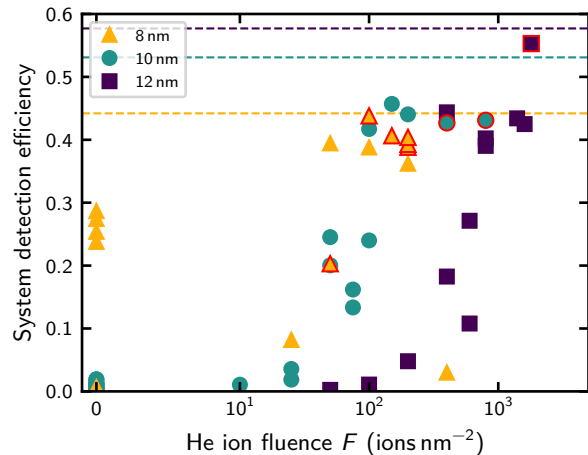


FIG. 3. System detection efficiency vs. He ion fluence for the three detector thicknesses studied in this work. Dashed lines indicate the absorption in the SNSPD simulated with FDTD; data points with saturating SDE are highlighted with a red frame. The relative uncertainties of SDE and He ion fluence are 2% and 5%, respectively (error bars not shown for clarity). Each of the data points stems from a different detector that was irradiated once with the given dose except for two 10 nm and two 12 nm detectors that were irradiated twice; for some SNSPDs we measured the SDE in addition also before irradiation. Despite the large scattering of data points that can be explained by the strong variation of the initial SDE between individual devices, one clearly sees that the SDE increases with He ion fluence and that the total maximum SDE is reached by the largest detector thickness.

thicknesses, despite the large scatter between data obtained from nominally identical SNSPDs. Most notably, the SDE for the 12 nm thick detectors increases from less than 0.05% for the non-irradiated case to 55.3% and just saturating detection efficiency for a fluence of 1800 ions nm^{-2} . As expected, the SDE increases with detector thickness due to the higher absorption. The dashed horizontal lines in Figure 3 show the upper limit for the SDE, defined by the absorption of SNSPDs of the respective thicknesses that we obtained from FDTD simulations discussed in Appendix A. We note that one can further enhance the absorption and thus the SDE over a broad wavelength range by adding a metal mirror with an optical cavity underneath the SNSPD.[57] Recently, a similar approach for He ion irradiated detectors involving a narrow-band cavity, realized with a distributed Bragg reflector, has shown to push the absorption to over 90%.[43] The fact that the measured SDE of the highest irradiated 8 nm detector shown in Figure 3 is less than 3% can be explained as follows: Due to the irradiation-induced reduction of the switching current (to 2.8 μA for this detector), which is also the maximum applicable bias current, the maximum voltage pulse amplitude decreases as well. However, the trigger level of the counter used to measure the efficiency can only be reduced correspond-

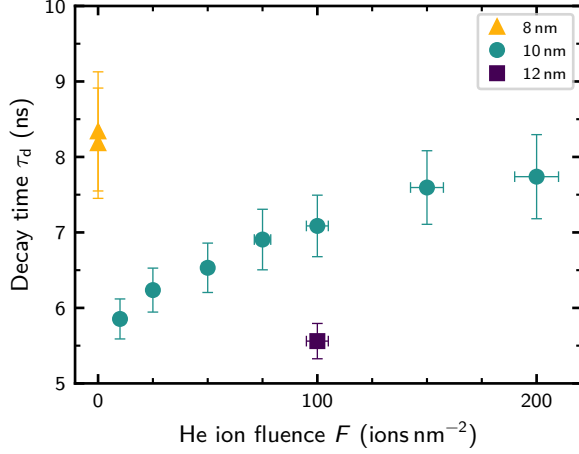


FIG. 4. Decay time vs. He ion fluence, including statistical errors. τ_d increases with increasing fluence and decreasing thickness due to the resulting higher kinetic inductance of the detector.

ingly as long as it is well above the electrical noise floor. This implies that once the pulse amplitude becomes comparable to the electrical noise floor, a substantial fraction of detection pulses will not be registered by the counter anymore. Depending on the readout electronics used and on their noise floor, this sets the limit for meaningful He ion fluences when irradiating SNSPDs. Surprisingly, one of the 12 nm/400 ions nm⁻² detectors shown in Figure 3 exhibits a high SDE although I_{sw} was lower than expected for these two SNSPDs. This hints to a relatively homogeneous current density within the nanowire that allows biasing close to the depairing current density and thus achieving high SDE.

Another key metric for SNSPDs is their recovery time since it determines the detector's maximum count rate. It can be estimated from the time constant τ_d of the exponential decay of a detection voltage pulse.[18, 58] Figure 4 shows how the measured decay time increases with increasing He ion fluence and demonstrates that it is smaller for thicker detectors. These observations can be understood as follows: The decay time depends on the kinetic inductance L_k of the detector by $\tau_d = L_k/R_{load}$ with a typical load resistance of $R_{load} = 50 \Omega$ for the readout electronics.[58] At the same time, L_k for a thin ($d \ll \lambda_{eff}$) and dirty ($\ell \ll \xi_0$) film of length l , width w , and thickness d is given by

$$L_k = \mu_0 \lambda_{eff,tf} \frac{l}{w}, \quad (1)$$

with the effective magnetic penetration depth for thin films $\lambda_{eff,tf} = \lambda_{eff}^2/d$ as introduced by Pearl [59], where λ_{eff} is the effective magnetic penetration depth of a dirty bulk superconductor like NbTiN, given by

$$\lambda_{eff} = \lambda_L \sqrt{\frac{\xi_0}{\ell}} = \sqrt{\frac{\hbar \rho}{\pi \mu_0 \Delta(0K)}} \quad (2)$$

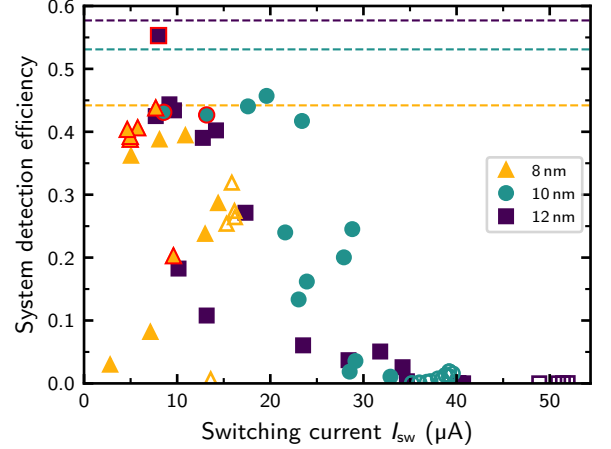


FIG. 5. Maximum system detection efficiency vs. switching current for the three detector thicknesses studied in this work. The simulated maximum SDE of each thickness is indicated by dashed lines, while saturating SDE is highlighted by symbols with a red frame; open symbols represent non-irradiated devices. The relative uncertainties of SDE and switching current are 2% and 6%, respectively (error bars not shown for clarity). Noteworthy are the data points at an SDE $\approx 45\%$, where the 10 nm SNSPDs provide a similar SDE like the 8 nm ones but offer the doubled switching current. Furthermore, for a similar I_{sw} of about 8 μA , one 12 nm SNSPD shows up to 55.3% SDE, whereas the 8 nm ones provide only up to 43.8% SDE.

according to Bartolf [60, Eq. (9.36)]. Here, λ_L is the London penetration depth, ξ_0 the BCS coherence length, ℓ the mean free path, ρ the specific resistivity of the superconducting film in the normal conducting state, and $\Delta(0K)$ the superconducting energy gap.[61] Hence, with the effective magnetic penetration depth one can express the kinetic inductance as

$$L_k = \mu_0 \frac{\lambda_{eff}^2}{d} \frac{l}{w} = \frac{\hbar R_{sheet}}{\pi \Delta(0K)} \frac{l}{w}. \quad (3)$$

Thus, for detectors of similar length and width, the kinetic inductance and the decay time are smaller for detectors that exhibit a smaller sheet resistance, for example due to the use of a thicker film or due to less irradiation with He ions. In this way, we conclude that the increase of decay time due to irradiation can be compensated to a certain extent by using thicker films.

For applications, simultaneously high SDE and I_{sw} are desired since a higher I_{sw} yields a higher detection pulse, which reduces not only the requirements for pulse detection with the readout electronics but also the timing jitter induced by electrical noise [16, 46]. To compare these two performance metrics, Figure 5 shows the SDE against I_{sw} (open symbols representing the non-irradiated detectors, a red frame highlighting saturating SDE, and dashed lines indicating the simulated SDE upper limit). It is interesting to note how I_{sw} and SDE compare between the 8 nm and the 10 nm devices with an SDE between 39%

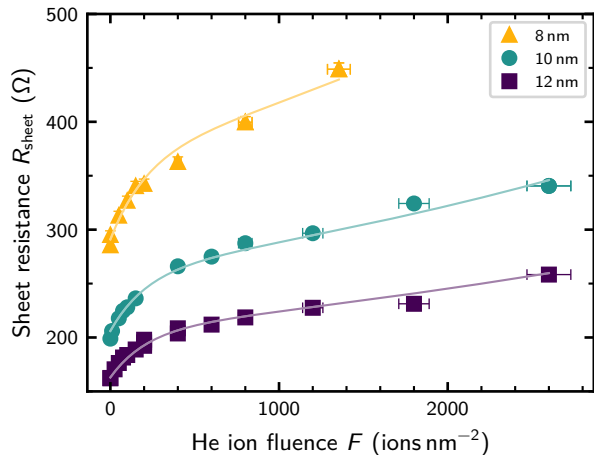


FIG. 6. Sheet resistance vs. He ion fluence for 8 nm, 10 nm, and 12 nm film thickness, including statistical errors. The sheet resistance increases with He ion fluence and decreasing film thickness. All three data sets are described by the fit function given by Equation (7) with the parameters of Table I.

and 46%: While providing a similar efficiency, the 10 nm devices offer twice as much switching current, 20 μA instead of 10 μA . This I_{sw} is also higher than that of the non-irradiated 8 nm detectors. Another comparison can be drawn between the 8 nm SNSPDs with saturating SDE close to 44% and the 12 nm SNSPD showing 55.3% SDE: at similar switching currents of about 8 μA , the 12 nm SNSPD provides a substantially higher SDE. Furthermore, it is noteworthy that the shift of the data point clouds in this two-dimensional parameter space is not monotonous to higher I_{sw} with higher thickness (except for the non-irradiated devices), which could hint to the existence of an optimum thickness between 8 nm and 12 nm to reach simultaneous high SDE and I_{sw} via He ion irradiation.

To conclude, by choosing a suitable detector thickness and He ion fluence, one can tune I_{sw} and SDE, even to better performance in both parameters simultaneously compared to non-irradiated detectors. Moreover, by individual irradiation of NbTiN SNSPDs with a suitable He ion fluence, one can intentionally modify the performance of selected detectors or even mitigate differences between nominally identical devices.

B. Scaling of thin film metrics with He ion fluence

To investigate how He ion irradiation impacts upon the bare NbTiN film metrics such as critical temperature T_c , sheet resistance R_{sheet} , and electron density n_e , we fabricated cloverleaf structures together with the detectors on the same sample to perform magneto-transport measurements in van-der-Pauw geometry. In Figure 6 we present the dependence of the sheet resistance R_{sheet} on the He ion fluence. As expected, R_{sheet} is higher for thinner

films and increases with increasing He ion fluence as the number of defects in the NbTiN film increases. Interestingly, the sheet resistance does not scale as $R_{\text{sheet}} = \rho/d_0$ with the nominal film thickness d_0 as expected if all samples had the same specific resistivity ρ . Even if one subtracts a 1.3 nm thick layer of oxidized NbTiN [52] from the nominal NbTiN thickness, the resulting resistivities of the non-irradiated films are still lower for the thicker films than for the 8 nm film (1.94 $\mu\Omega\text{m}$, 1.73 $\mu\Omega\text{m}$, and 1.73 Ωm for the 8 nm, 10 nm, and 12 nm films, respectively). Although one might expect R_{sheet} to saturate at high fluences due to a saturating defect density in the film, we experimentally observe a continuous increase of R_{sheet} with He ion fluence. This could have its origin in noticeable surface sputtering [62] and intermixing [63] at the film/substrate interface by the impinging He ions and an associated reduction of the effective film thickness.

Based on these observations and taking the sheet resistance to be directly proportional to the defect density, we develop a simple physical model. In our model, each ion that passes through the film can create a defect cluster of an average volume v_D with an efficiency η . Moreover, we consider the film volume V as divided into many volume elements with the same size as the average defect cluster volume v_D , and defect clusters may only be created in volume elements that do not already contain a defect cluster. Those considerations imply that irradiating a film of volume V , thickness d , and area A using a He ion fluence ΔF creates ΔN_D new defect clusters according to

$$\Delta N_D = \left(\frac{V - N_D v_D}{V} \right) \left(\frac{d}{\sqrt[3]{v_D}} \right) \eta A \Delta F. \quad (4)$$

The first fraction represents the fraction of V that does not yet contain defect clusters, the second fraction represents the number of potential defect clusters that an impinging ion could create when passing the film along its thickness. Dividing this equation by the total volume V to obtain an expression for the defect cluster density n_D and taking the limit $\Delta F \rightarrow 0$ yields

$$\frac{dn_D}{dF} = \frac{\eta}{\sqrt[3]{v_D}} (1 - v_D n_D(F)). \quad (5)$$

This differential equation has the solution

$$n_D(F) = \frac{1}{v_D} \left(1 - (1 - n_{D,0} v_D) e^{-\eta v_D^{2/3} F} \right), \quad (6)$$

where $n_{D,0}$ is the defect cluster density of the non-irradiated film. We relate the defect cluster density to the specific resistivity ρ via direct proportionality with a film-thickness dependent constant a_{d_0} . To arrive at a model for the sheet resistance, we further account for the previously mentioned surface sputtering due to He ion bombardment by including an effective reduction of the original film thickness d_0 with a sputtering rate r_s and

conclude

$$R_{\text{sheet}}(F) = \frac{1}{v_D} \left(1 - (1 - n_{D,0} v_D) e^{-\eta v_D^{2/3} F} \right) \frac{a_{d_0}}{d_0 - r_s F}. \quad (7)$$

We fit this model to the experimental data and present the results of this fitting in Figure 6. Since the sputtering rate r_s and the factors $n_{D,0} v_D$ and $\eta v_D^{2/3}$ contain only thickness-independent quantities, we choose these factors as common fit parameters for all three thicknesses. In this way, a_{d_0}/v_D is the only individual fit parameter for each thickness, while the other three previously mentioned parameters are shared between all films. As such, we fit the three data sets with six parameters. Table I lists the parameters that result in the fit functions shown in Figure 6. Considering the volume V as divided into many volume elements with the same size as the average defect cluster volume v_D , the parameter $n_{D,0} v_D$ can be qualitatively interpreted as the fraction of volume elements of the non-irradiated film that contains transport-related defective regions such as grain boundaries and scattering centers. We obtain $n_{D,0} v_D = 0.79$, indicating that the initial defect cluster density is large and/or the average volume of a defect cluster induced by a single He ion collision is on the order of the NbTiN grain size. A high defect density is not unexpected for a polycrystalline material such as NbTiN, and a defect cascade induced by a single He ion can extend over a volume similar to the NbTiN grain size (few nm) according to a study of He ion irradiation induced defect clusters in copper [64]. Furthermore, the quantity $\eta v_D^{2/3}$ can be understood as the cross section determining the probability that an impinging He ion creates a defect cluster of volume v_D . Moreover, the sputtering rate of $9.4 \times 10^{-4} \text{ nm}/(\text{ions}/\text{nm}^2)$ implies that an irradiation by $1000 \text{ ions}/\text{nm}^2$ leads to an effective reduction of the NbTiN film thickness by about 1 nm. Although Zhang *et al.* [42] did not observe a change in thickness after irradiating their NbN film with $500 \text{ ions}/\text{nm}^2$, our observation agrees well with the simulated and experimentally observed sputtering yield of typically 1 nm per $1000 \text{ ions}/\text{nm}^2$ found in literature [62, 65].

Figure 7 shows the dependence of the critical temperature T_c on the He ion fluence for 8 nm, 10 nm, and 12 nm thick films. Clearly, T_c decreases continuously by about 30% from the non-irradiated film to the film irradiated with $1200 \text{ ions}/\text{nm}^2$. Similarly to R_{sheet} , also T_c decreases most strongly for small He ion fluences. Interestingly, the measured values of T_c for the 10 nm and 12 nm films are very similar for low He ion fluences, although we would expect a lower T_c for the thinner film due to the suppression of superconducting properties when transitioning from bulk to the nanoscale. [67–69] Furthermore, we fit our experimental data for T_c and R_{sheet} with the universal scaling law introduced by Ivry *et al.* [66], $d_0 T_c = A R_{\text{sheet}}^{-B}$, which relates critical temperature, sheet resistance, and film thickness. Combining then the resulting fit function $T_c(R_{\text{sheet}}, d_0)$ with our

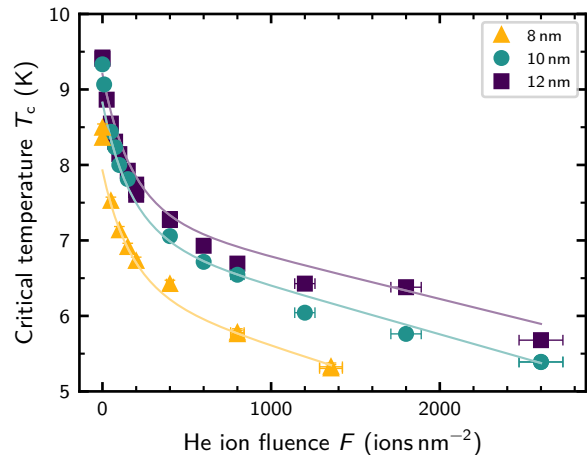


FIG. 7. Critical temperature vs. He ion fluence, including statistical errors. T_c decreases with He ion fluence, with the reduction in T_c at small fluences being the strongest. Surprisingly, T_c for the unirradiated 10 nm and 12 nm films are similar for small fluences, although T_c is typically higher for thicker films. The continuous functions we determined by fitting the T_c and R_{sheet} data with the universal scaling law introduced by Ivry *et al.* [66], $d_0 T_c = A R_{\text{sheet}}^{-B}$, and subsequently using our physical model for R_{sheet} , given by Equation (7), as input to the universal scaling law.

physical fit function for R_{sheet} , Equation (7), we obtain the fits shown in Figure 7. Appendix C contains details of the fitting procedure used for T_c . A recent publication by Ruhtinas and Maasilta [70] contains a study of the critical temperature and the critical current density of comparably thick, 35 nm and 100 nm, NbTiN bridges, in which they suppressed superconductivity by He ion irradiation of a narrow line perpendicular to the bridge. Empirically, they observed a logarithmic dependence of T_c and an exponential dependence of j_{sw} on the He ion fluence F . For the critical temperature, a fit of our data with $T_c(F) = -a \log(F+b) + c$ and fitting parameters a , b , and c for each of the three thicknesses describes our data even a bit better than the universal scaling law. However, using the universal scaling law, we need only the two fitting parameters A and B to describe all three data sets, while the empirical logarithmic fit function requires three fitting parameters for each thickness, a total of nine parameters for our three data sets. Moreover, our data for j_{sw} as shown in the inset of Figure 2 indicates that the switching current density does not follow the exponential dependence observed by Ruhtinas and Maasilta [70], especially for the smaller He ion fluences. However, we note that compared to our work, Ruhtinas and Maasilta [70] studied the switching current density for higher fluences, ranging from $2 \times 10^4 \text{ ions}/\text{nm}^2$ to $12 \times 10^4 \text{ ions}/\text{nm}^2$. Furthermore, since the film thickness has a strong influence on T_c , an interesting question is how the detectors' T_c compares between a thicker, higher irradiated SNSPD with a thinner, lower irradiated detector that both show

TABLE I. Fit parameters of the physical model according to Equation (7), describing the data in Figure 6. For each thickness, the fit function has its own fit parameter a_{d_0}/v_D , while the other parameters are independent of film thickness and therefore shared between the three fit functions.

d_0 (nm)	a_{d_0}/v_D (Ω)	$n_{D,0} v_D$ (1)	$\eta v_D^{2/3}$ (nm^2)	r_s ($\text{nm}/(\text{ions}/\text{nm}^2)$)
8	2957 ± 36			
10	2618 ± 36	0.79 ± 0.01	$(4.7 \pm 0.7) \times 10^{-3}$	$(9.4 \pm 0.6) \times 10^{-4}$
12	2484 ± 32			

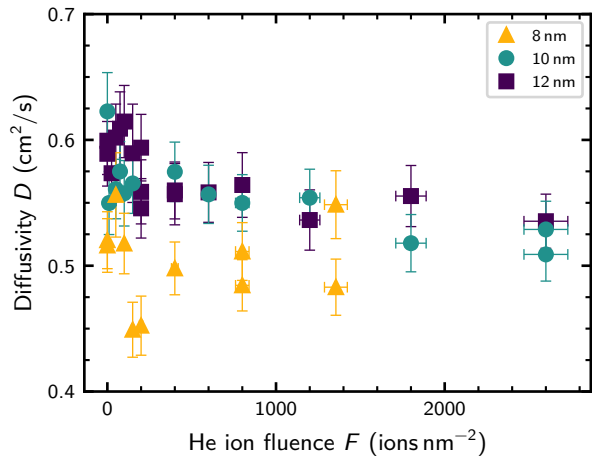


FIG. 8. Quasiparticle diffusivity vs. He ion fluence, including statistical errors. D is almost constant within the error bars, and averaging over all fluences reveals the thickness dependence of D . One might see a slight decrease of D with increasing fluence, which could be explained by the thickness reduction due to sputtering during He ion irradiation and the thickness dependence of D .

a similar SDE. As elaborated in Appendix B, our data suggests that with the 10 nm detectors one can reach a similar SDE as with the 8 nm thick SNSPDs, while retaining a T_c of 8 K instead of 7.5 K. This is especially useful for applications with limited cooling powers.

Next, we discuss measurements of the quasiparticle diffusivity D . For this, we measured the temperature dependence of the upper critical magnetic field $B_{c2}(T)$ by performing magneto-transport measurements while varying the temperature. From linear fits of $B_{c2}(T)$ close to T_c , we extract the slope dB_{c2}/dT and calculate the diffusivity [50]

$$D = \frac{4k_B}{\pi e} \left[\frac{dB_{c2}}{dT} \right]_{T \rightarrow T_c}^{-1}. \quad (8)$$

Magnetic field sweeps were also performed with the film in the normal conducting state and at constant temperature, while measuring the Hall voltage V_H . Since V_H varies linearly with the applied magnetic field B and measurement current I , we determine the Hall coefficient $R_H = V_H d_0 / (IB)$ using the slope of a linear fit of the $V_H(B)$ data. From this, we estimate the electron den-

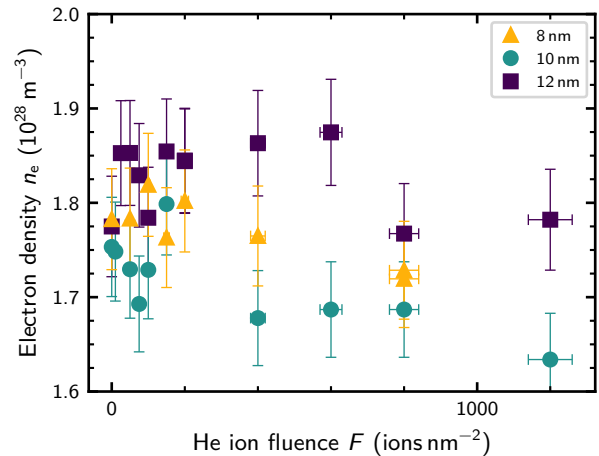


FIG. 9. Electron density vs. He ion fluence, including statistical errors. Despite fluctuations between measurements, n_e seems almost constant. One might see a slight decrease with increasing He ion fluence, which could be explained by the thickness dependence of n_e and the reduction of the effective film thickness during irradiation due to sputtering.

sity n_e according to $R_H = -1/(n_e e)$ within the free electron model (see also [49, 50, 71]). Figures 8 and 9 show the quasiparticle diffusivity and the electron density as a function of the He ion fluence. Both are almost constant within the experimental error bars, although one might see a slight decrease of the diffusivity and the electron density with increasing He ion fluence. Since we usually observe decreasing electron density and diffusivity with decreasing film thickness like Sidorova *et al.* [49], this may be related to the observed effective thickness reduction of 0.94 nm per 1000 ions nm^{-2} due to sputtering during He ion irradiation.

IV. CONCLUSION AND OUTLOOK

In summary, we used a He ion microscope to locally tune the performance metrics of individual SNSPDs fabricated on the same chip. At the same time, our results demonstrated the possibilities of using thick (up to 12 nm) NbTiN films and He ion irradiation to enhance performance metrics such as system detection efficiency, switching current, decay time, and operating temperature compared to SNSPDs of smaller thicknesses.

Thicker detectors exhibit higher optical absorption efficiency and shorter decay times as compared to similar SNSPDs fabricated from thinner films. However, due to the reduction of single-photon sensitivity with detector thickness, such SNSPDs typically offer only small detection efficiencies. Here, we have shown how He ion irradiation can boost the initially negligible SDE ($< 0.05\%$) of 12 nm thick SNSPDs at 4.5 K by three orders of magnitude to 55.3%, resulting in an internal detection efficiency just within the saturated regime. This enables the use of thicker films and the associated advantages—at temperatures reachable with standard pulse-tube or Gifford-McMahon cryocoolers.[72] Furthermore, we found that by combining He ion irradiation and detectors fabricated from thicker films, one can enhance SDE and I_{sw} while reducing the decay time compared to non-irradiated smaller-thickness SNSPDs. While reduced decay times result in increased maximum count rates, higher I_{sw} and the associated higher detection voltage pulse imply a higher signal-to-noise ratio, which reduces the electrical noise induced timing jitter [16] and the necessary amplification of the electrical readout circuit.

Using a He ion microscope to irradiate individual detectors and cloverleaf structures on the same chip with different fluences allowed us to precisely study SNSPD and film properties over He ion fluences ranging from 0 ions nm^{-2} to 2600 ions nm^{-2} , avoiding any errors that could arise from the high sensitivity of device properties on the exact sputtering or the subsequent fabrication process. We found that the increase of sheet resistance with the He ion fluence can be well described by a simple physical model that includes defect generation in the NbTiN film and an effective reduction of thickness due to sputtering during He ion bombardment. Moreover, the decrease of critical temperature with the He ion fluence can be described by combining our physical model for R_{sheet} with the universal scaling law from Ivry *et al.* [66], which relates critical temperature, film thickness, and sheet resistance. At the same time, the quasiparticle diffusivity and electron density stay almost constant for the He ion fluences studied in this work. These magneto-transport measurements also show that irradiation of SNSPDs with He ions continuously changes their properties—although one can employ irradiation to enhance the SNSPD performance, excessive He ion irradiation ultimately leads to a vanishing, non-detectable signal when a photon is absorbed, rendering the SNSPD inoperative. These findings could be particularly interesting for applications where SNSPDs are exposed to radiation and high-energy particles.[25]

Besides the general enhancement of performance metrics of NbTiN SNSPDs by using thicker films combined with He ion irradiation, one can use targeted irradiation of individual devices with a He ion microscope for example in large SNSPD arrays to mitigate inhomogeneities of detector performance between pixels (or even dark pixels). This would be challenging without a post-processing

technique such as site-selective He ion irradiation. Furthermore, targeted He ion irradiation enables the optimization of detectors for different performance metrics on the same chip, also after fabrication.

ACKNOWLEDGMENTS

The authors thank Kirill Fedorov and Stefan Appel for helpful discussions. We gratefully acknowledge support from the German Federal Ministry of Education and Research (BMBF) via the projects PhotonQ (13N15760), SPINNING (13N16214), MARQUAND (BN105022), and “Photonics Research Germany” (13N14846), via the funding program “Quantum technologies – from basic research to market” (16K1SQ033, 13N15855, and 13N15982), as well as from the German Research Foundation (DFG) under Germany’s Excellence Strategy EXC-2111 (390814868) and projects INST 95/1220-1 (MQCL) and INST 95/1654-1 FUGG. This research is part of the “Munich Quantum Valley”, which is supported by the Bavarian state government with funds from the “High-tech Agenda Bayern Plus”.

Appendix A: Simulation of optical absorption in SNSPDs

The optical absorption in a detector provides an upper limit for its SDE. To determine the absorption for the detectors fabricated in this work, we performed finite-difference time domain (FDTD) simulations (Ansys Lumerical). Input parameters for these simulations are the width and thickness of the nanowire and the optical constants of the superconducting film that provides the basis for the detectors. We controlled the thickness of the films by measuring the sputter deposition rate and selecting the deposition time accordingly. The optical constants were measured with a variable angle spectroscopic ellipsometer (M-2000, J.A. Woollam Co.). After detector fabrication, we evaluated the width of 22 representative detectors (Genesys ProSEM) and determined their mean wire width as listed in Table II. Moreover, for the simulations we chose a plane-wave source with its polarization parallel to the nanowire, in line with the experiment. Table II shows the simulation input parameters and results for the optical absorption of the detectors of this work. The design of all detectors consists of 100 nm wide wires and a fill factor of 50% as described in Section II. The measured width of the fabricated detectors deviates from this nominal value due to slight under-/overexposure during electron-beam lithography. This, however, does not change the reasoning within this work: For the same pitch, increased wire width (increased fill factor) or increased thickness both increase optical absorption and switching current, while reducing the detector’s sensitivity to single photons.

TABLE II. Simulation parameters and results for the absorption in the 8 nm, 10 nm, and 12 nm thick detectors of this work. d_0 is the nominal thickness of the detector, while w represents its mean wire width. n and k are refractive index and extinction coefficient, respectively. The absorption fraction α denotes the percentage of light that is absorbed in the detector, obtained from FDTD simulations.

d_0 (nm)	w (nm)	n (1)	k (1)	α (%)
8	92.6 ± 4.0	2.47	3.18	44.2
10	107.3 ± 1.9	2.48	3.33	53.1
12	115.3 ± 3.4	2.48	3.54	57.7

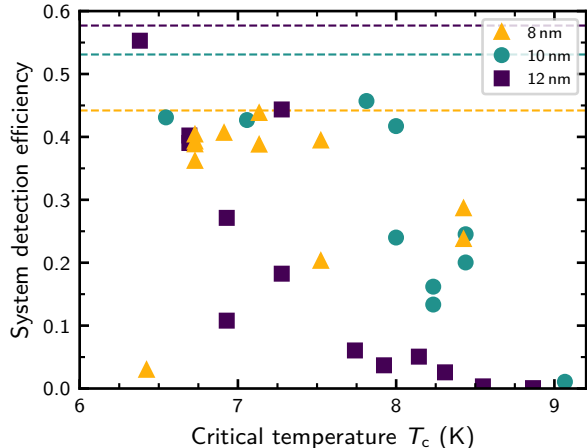


FIG. 10. SDE of differently irradiated SNSPDs vs. T_c of corresponding CLs of three different thicknesses. The relative uncertainty of the SDE is 2%, the uncertainty of the temperature amounts to 50 mK (error bars not shown for clarity).

Appendix B: Comparison of T_c and SDE

The critical temperature T_c of SNSPDs is especially important for applications with limited cooling capabilities. In this section, we address the question how T_c compares between thicker, higher irradiated detectors and thinner, lower irradiated SNSPDs that both show a similar SDE. For this, we compare the detector's SDE with the thin-film T_c in Figure 10. The data suggests that with 44% the 10 nm detectors can actually reach an SDE comparable to the 8 nm SNSPDs, while retaining a T_c of 8 K instead of 7.5 K. This can be particularly useful for applications because a higher T_c reduces the requirements for the cooling system to operate the SNSPDs.

Appendix C: Fitting of T_c with universal scaling law

To describe the data for the critical temperature in Figure 7, we use the universal scaling law, introduced by Ivry *et al.* [66],

$$dT_c = AR_{\text{sheet}}^{-B}, \quad (\text{C1})$$

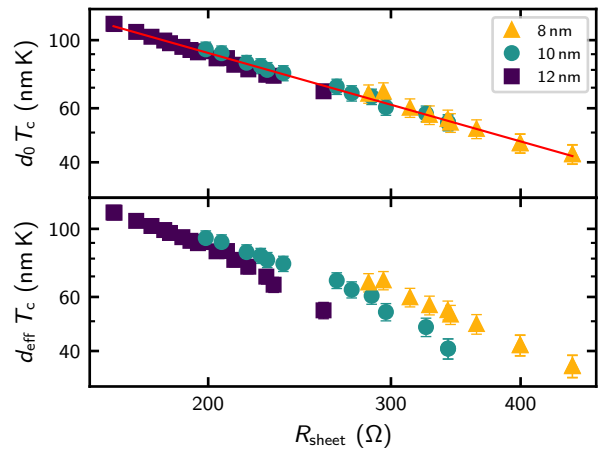


FIG. 11. Critical temperature multiplied with film thickness vs. sheet resistance, including statistical errors. In the upper plot the thickness of the non-irradiated film is used, while the effective thickness used in the lower plot accounts for surface sputtering and intermixing at the film/substrate interface due to He ion irradiation. The red line in the upper plot is a fit according to the universal scaling law introduced by Ivry *et al.* [66], $d_0T_c = AR_{\text{sheet}}^{-B}$.

which relates film thickness, critical temperature, and sheet resistance. Figure 11 shows the critical temperature, multiplied with the thickness of the non-irradiated film, d_0T_c . Evidently, this quantity exhibits a linear dependence on the sheet resistance on a log-log scale. As the data of the differently irradiated 8 nm, 10 nm, and 12 nm thick films approximately collapse on a single line, we choose one joint fitting function to determine the constants A and B of the universal scaling law and obtain the unitless constants $A = 1.44 \times 10^4$ and $B = 0.957$, provided that the data for d , T_c , and R_{sheet} are given in nm, K, and Ω , respectively. With these parameters, we obtain the fitting functions shown in Figure 7.

It is interesting to note that the linearity of the three data sets shown in the upper part of Figure 11 is lost when multiplying T_c with the effective thickness $d_{\text{eff}} = d_0 - r_s F$ instead of the thickness before irradiation, as shown in the lower part of Figure 11. As introduced in Section III B, this reduction of the effective thickness by 0.94 nm per 1000 ions nm^{-2} accounts for surface sputtering and intermixing at the film/substrate interface. At present, we can only give a qualitative explanation why the effective thickness is important to describe the continuous increase of R_{sheet} in Figure 6 and why it is not relevant for describing T_c : Via AFM measurements, we observed a surface roughening by He ion irradiation due to surface sputtering and redeposition. Considering now a thin slab of the rough surface, parallel to the sample plane, it consists of many connected islands of NbTiN (or an oxide thereof). On the one hand, this slab has a higher resistivity in the normal conducting state due to the voids; on the other hand, it should have a T_c

similar to a slab without voids as long as the voids are smaller than the coherence length of the superconductor. Of course, further investigation is necessary to better understand the role of surface sputtering and intermixing

at the film/substrate interface as well as their influence on thickness, sheet resistance, and critical temperature of the thin film.

-
- [1] G. N. Gol'tsman, O. Okunev, G. Chulkova, A. Lipatov, A. Semenov, K. Smirnov, B. Voronov, A. Dzardanov, C. Williams, and R. Sobolewski, Picosecond superconducting single-photon optical detector, *Applied Physics Letters* **79**, 705 (2001).
- [2] H. Takesue, S. W. Nam, Q. Zhang, R. H. Hadfield, T. Honjo, K. Tamaki, and Y. Yamamoto, Quantum key distribution over a 40-dB channel loss using superconducting single-photon detectors, *Nature Photonics* **1**, 343 (2007).
- [3] J.-P. Chen, C. Zhang, Y. Liu, C. Jiang, D.-F. Zhao, W.-J. Zhang, F.-X. Chen, H. Li, L.-X. You, Z. Wang, Y. Chen, X.-B. Wang, Q. Zhang, and J.-W. Pan, Quantum Key Distribution over 658 km Fiber with Distributed Vibration Sensing, *Physical Review Letters* **128**, 180502 (2022).
- [4] Y. Liu, W.-J. Zhang, C. Jiang, J.-P. Chen, C. Zhang, W.-X. Pan, D. Ma, H. Dong, J.-M. Xiong, C.-J. Zhang, H. Li, R.-C. Wang, J. Wu, T.-Y. Chen, L. You, X.-B. Wang, Q. Zhang, and J.-W. Pan, Experimental Twin-Field Quantum Key Distribution Over 1000 km Fiber Distance (2023), arxiv:2303.15795 [quant-ph].
- [5] F. Bussi eres, C. Clausen, A. Tiranov, B. Korzh, V. B. Verma, S. W. Nam, F. Marsili, A. Ferrier, P. Goldner, H. Herrmann, C. Silberhorn, W. Sohler, M. Afzelius, and N. Gisin, Quantum teleportation from a telecom-wavelength photon to a solid-state quantum memory, *Nature Photonics* **8**, 775 (2014).
- [6] A. McCarthy, N. J. Krichel, N. R. Gemmell, X. Ren, M. G. Tanner, S. N. Dorenbos, V. Zwiller, R. H. Hadfield, and G. S. Buller, Kilometer-range, high resolution depth imaging via 1560 nm wavelength single-photon detection, *Optics Express* **21**, 8904 (2013).
- [7] M. E. Grein, A. J. Kerman, E. A. Dauler, M. M. Willis, B. Romkey, R. J. Molnar, B. S. Robinson, D. V. Murphy, and D. M. Boroson, An optical receiver for the Lunar Laser Communication Demonstration based on photon-counting superconducting nanowires, *Advanced Photon Counting Techniques IX* **9492**, 949208 (2015).
- [8] H. Takesue, S. D. Dyer, M. J. Stevens, V. Verma, R. P. Mirin, and S. W. Nam, Quantum teleportation over 100 km of fiber using highly efficient superconducting nanowire single-photon detectors, *Optica* **2**, 832 (2015).
- [9] R. Valivarthi, M. G. Puigibert, Q. Zhou, G. H. Aguilar, V. B. Verma, F. Marsili, M. D. Shaw, S. W. Nam, D. Oblak, and W. Tittel, Quantum teleportation across a metropolitan fibre network, *Nature Photonics* **10**, 676 (2016).
- [10] J. Zhang, N. Boiadjeva, G. Chulkova, H. Deslandes, G. Gol'tsman, A. Korneev, P. Kouminov, M. Leibowitz, W. Lo, R. Malinsky, O. Okunev, A. Pearlman, W. Slysz, K. Smirnov, C. Tsao, A. Verevkin, B. Voronov, K. Wilsher, and R. Sobolewski, Noninvasive CMOS circuit testing with NbN superconducting single-photon detectors, *Electronics Letters* **39**, 1086 (2003).
- [11] M. G. Tanner, S. D. Dyer, B. Baek, R. H. Hadfield, and S. Woo Nam, High-resolution single-mode fiber-optic distributed Raman sensor for absolute temperature measurement using superconducting nanowire single-photon detectors, *Applied Physics Letters* **99**, 201110 (2011).
- [12] M. A. Itzler, X. Jiang, M. Entwistle, K. Slomkowski, A. Tosi, F. Acerbi, F. Zappa, and S. Cova, Advances in InGaAsP-based avalanche diode single photon detectors, *Journal of Modern Optics* **58**, 174 (2011).
- [13] F. Marsili, F. Bellei, F. Najafi, A. E. Dane, E. A. Dauler, R. J. Molnar, and K. K. Berggren, Efficient Single Photon Detection from 500nm to 5µm Wavelength, *Nano Letters* **12**, 4799 (2012).
- [14] A. Korneev, Yu. Korneeva, I. Florya, B. Voronov, and G. Goltsman, NbN Nanowire Superconducting Single-Photon Detector for Mid-Infrared, *Physics Procedia* **36**, 72 (2012).
- [15] H. Shibata, K. Shimizu, H. Takesue, and Y. Tokura, Ultimate low system dark-count rate for superconducting nanowire single-photon detector, *Optics Letters* **40**, 3428 (2015).
- [16] B. Korzh, Q. Y. Zhao, J. P. Allmaras, S. Frasca, T. M. Autry, E. A. Bersin, A. D. Beyer, R. M. Briggs, B. Bumble, M. Colangelo, G. M. Crouch, A. E. Dane, T. Gerrits, A. E. Lita, F. Marsili, G. Moody, C. Pe a, E. Ramirez, J. D. Rezac, N. Sinclair, M. J. Stevens, A. E. Velasco, V. B. Verma, E. E. Wollman, S. Xie, D. Zhu, P. D. Hale, M. Spiropulu, K. L. Silverman, R. P. Mirin, S. W. Nam, A. G. Kozorezov, M. D. Shaw, and K. K. Berggren, Demonstration of sub-3 ps temporal resolution with a superconducting nanowire single-photon detector, *Nature Photonics* **14**, 250 (2020).
- [17] C. M. Natarajan, M. G. Tanner, and R. H. Hadfield, Superconducting nanowire single-photon detectors: Physics and applications, *Superconductor Science and Technology* **25**, 063001 (2012).
- [18] S. Ferrari, C. Schuck, and W. Pernice, Waveguide-integrated superconducting nanowire single-photon detectors, *Nanophotonics* **7**, 1725 (2018).
- [19] J. P. Sprengers, A. Gaggero, D. Sahin, S. Jahanmirinejad, G. Frucci, F. Mattioli, R. Leoni, J. Beetz, M. Lerner, M. Kamp, S. H ofling, R. Sanjines, and A. Fiore, Waveguide superconducting single-photon detectors for integrated quantum photonic circuits, *Applied Physics Letters* **99**, 181110 (2011).
- [20] G. Reithmaier, S. Lichtmannecker, T. Reichert, P. Hasch, K. M uller, M. Bichler, R. Gross, and J. J. Finley, On-chip time resolved detection of quantum dot emission using integrated superconducting single photon detectors, *Scientific Reports* **3**, 1901 (2013).
- [21] G. Reithmaier, M. Kaniber, F. Flassig, S. Lichtmannecker, K. M uller, A. Andrejew, J. Vu kovi c, R. Gross, and J. J. Finley, On-Chip Generation, Routing, and Detection of Resonance Fluorescence, *Nano Letters* **15**, 5208 (2015).

- [22] S. Majety, S. Strohauser, P. Saha, F. Wietschorke, J. J. Finley, K. Müller, and M. Radulaski, Triangular quantum photonic devices with integrated detectors in silicon carbide, *Materials for Quantum Technology* **3**, 015004 (2023).
- [23] E. E. Wollman, V. B. Verma, A. B. Walter, J. Chiles, B. Korzh, J. P. Allmaras, Y. Zhai, A. E. Lita, A. N. McCaughan, E. Schmidt, S. Frasca, R. P. Mirin, S. W. Nam, and M. D. Shaw, Recent advances in superconducting nanowire single-photon detector technology for exoplanet transit spectroscopy in the mid-infrared, *Journal of Astronomical Telescopes, Instruments, and Systems* **7**, 011004 (2021).
- [24] J. Chiles, I. Charaev, R. Lasenby, M. Baryakhtar, J. Huang, A. Roshko, G. Burton, M. Colangelo, K. Van Tilburg, A. Arvanitaki, S. W. Nam, and K. K. Berggren, New Constraints on Dark Photon Dark Matter with Superconducting Nanowire Detectors in an Optical Haloscope, *Physical Review Letters* **128**, 231802 (2022).
- [25] T. Polakovic, W. Armstrong, G. Karapetrov, Z. E. Meziani, and V. Novosad, Unconventional applications of superconducting nanowire single photon detectors, *Nanomaterials* **10**, 1198 (2020).
- [26] M. Shigefuji, A. Osada, M. Yabuno, S. Miki, H. Terai, and A. Noguchi, Efficient low-energy single-electron detection using a large-area superconducting microstrip (2023), arxiv:2301.11212 [cond-mat, physics:physics, physics:quant-ph].
- [27] E. E. Wollman, V. B. Verma, A. E. Lita, W. H. Farr, M. D. Shaw, R. P. Mirin, and S. Woo Nam, Kilopixel array of superconducting nanowire single-photon detectors, *Optics Express* **27**, 35279 (2019).
- [28] A. N. McCaughan, Y. Zhai, B. Korzh, J. P. Allmaras, B. G. Oripov, M. D. Shaw, and S. W. Nam, The thermally coupled imager: A scalable readout architecture for superconducting nanowire single photon detectors, *Applied Physics Letters* **121**, 102602 (2022).
- [29] H. L. Hortensius, E. F. C. Driessen, and T. M. Klapwijk, Possible Indications of Electronic Inhomogeneities in Superconducting Nanowire Detectors, *IEEE Transactions on Applied Superconductivity* **23**, 2200705 (2013).
- [30] Y. Noat, V. Cherkez, C. Brun, T. Cren, C. Carbillat, F. Debontridder, K. Ilin, M. Siegel, A. Semenov, H.-W. Hübers, and D. Roditchev, Unconventional superconductivity in ultrathin superconducting NbN films studied by scanning tunneling spectroscopy, *Physical Review B* **88**, 014503 (2013).
- [31] B. Sacépé, C. Chapelier, T. I. Baturina, V. M. Vinokur, M. R. Baklanov, and M. Sanquer, Disorder-Induced Inhomogeneities of the Superconducting State Close to the Superconductor-Insulator Transition, *Physical Review Letters* **101**, 157006 (2008).
- [32] J. R. Kirtley, S. I. Raider, R. M. Feenstra, and A. P. Fein, Spatial variation of the observed energy gap in granular superconducting NbN films, *Applied Physics Letters* **50**, 1607 (1987).
- [33] M. S. Allman, V. B. Verma, M. Stevens, T. Gerrits, R. D. Horansky, A. E. Lita, F. Marsili, A. Beyer, M. D. Shaw, D. Kumor, R. Mirin, and S. W. Nam, A near-infrared 64-pixel superconducting nanowire single photon detector array with integrated multiplexed readout, *Applied Physics Letters* **106**, 192601 (2015).
- [34] R. Gaudio, K. P. M. op 't Hoog, Z. Zhou, D. Sahin, and A. Fiore, Inhomogeneous critical current in nanowire superconducting single-photon detectors, *Applied Physics Letters* **105**, 222602 (2014).
- [35] A. J. Kerman, E. A. Dauler, J. K. Yang, K. M. Rosfjord, V. Anant, K. K. Berggren, G. N. Gol'tsman, and B. M. Voronov, Constriction-limited detection efficiency of superconducting nanowire single-photon detectors, *Applied Physics Letters* **90**, 101110 (2007).
- [36] I. Esmaeil Zadeh, J. Chang, J. W. Los, S. Gyger, A. W. Elshaari, S. Steinhauer, S. N. Dorenbos, and V. Zwiller, Superconducting nanowire single-photon detectors: A perspective on evolution, state-of-the-art, future developments, and applications, *Applied Physics Letters* **118**, 190502 (2021).
- [37] F. Marsili, V. B. Verma, J. A. Stern, S. Harrington, A. E. Lita, T. Gerrits, I. Vayshenker, B. Baek, M. D. Shaw, R. P. Mirin, and S. W. Nam, Detecting single infrared photons with 93% system efficiency, *Nature Photonics* **7**, 210 (2013).
- [38] S. Steinhauer, S. Gyger, and V. Zwiller, Progress on large-scale superconducting nanowire single-photon detectors, *Applied Physics Letters* **118**, 100501 (2021).
- [39] R. Cheng, S. Wang, and H. X. Tang, Superconducting nanowire single-photon detectors fabricated from atomic-layer-deposited NbN, *Applied Physics Letters* **115**, 241101 (2019).
- [40] E. Knehr, A. Kuzmin, D. Y. Vodolazov, M. Ziegler, S. Doerner, K. Ilin, M. Siegel, R. Stolz, and H. Schmidt, Nanowire single-photon detectors made of atomic layer-deposited niobium nitride, *Superconductor Science and Technology* **32**, 125007 (2019).
- [41] R. Cheng, J. Wright, H. G. Xing, D. Jena, and H. X. Tang, Epitaxial niobium nitride superconducting nanowire single-photon detectors, *Applied Physics Letters* **117**, 132601 (2020).
- [42] W. Zhang, Q. Jia, L. You, X. Ou, H. Huang, L. Zhang, H. Li, Z. Wang, and X. Xie, Saturating Intrinsic Detection Efficiency of Superconducting Nanowire Single-Photon Detectors via Defect Engineering, *Physical Review Applied* **12**, 044040 (2019).
- [43] G.-Z. Xu, W.-J. Zhang, L.-X. You, J.-M. Xiong, X.-Q. Sun, H. Huang, X. Ou, Y.-M. Pan, C.-L. Lv, H. Li, Z. Wang, and X.-M. Xie, Superconducting microstrip single-photon detector with system detection efficiency over 90% at 1550 nm, *Photonics Research* **9**, 958 (2021).
- [44] W.-J. Zhang, G.-Z. Xu, L.-X. You, C.-J. Zhang, H. Huang, X. Ou, X.-Q. Sun, J.-M. Xiong, H. Li, Z. Wang, and X.-M. Xie, Sixteen-channel fiber array-coupled superconducting single-photon detector array with average system detection efficiency over 60% at telecom wavelength, *Optics Letters* **46**, 1049 (2021).
- [45] X. Zhang, W. Zhang, H. Zhou, X. Zhang, L. You, H. Li, D. Fan, Y. Pan, H. Yu, L. Li, and Z. Wang, NbN Superconducting Nanowire Single-Photon Detector with 90.5% Saturated System Detection Efficiency and 14.7 ps System Jitter at 1550 nm Wavelength, *IEEE Journal of Selected Topics in Quantum Electronics* **28**, 1 (2022).
- [46] R. Flaschmann, L. Zugliani, C. Schmid, S. Spedicato, S. Strohauser, F. Wietschorke, F. Flassig, J. J. Finley, and K. Müller, The dependence of timing jitter of superconducting nanowire single-photon detectors on the multi-layer sample design and slew rate, *Nanoscale* **15**, 1086 (2023).
- [47] L. J. van der Pauw, A method of measuring the resistivity and Hall coefficient on lamellae of arbitrary shape,

- Philips Technical Review **20**, 220 (1958).
- [48] I. Miccoli, F. Edler, H. Pfnür, and C. Tegenkamp, The 100th anniversary of the four-point probe technique: The role of probe geometries in isotropic and anisotropic systems, *Journal of Physics: Condensed Matter* **27**, 223201 (2015).
- [49] M. Sidorova, A. D. Semenov, H. W. Hübers, S. Gyger, S. Steinhauer, X. Zhang, and A. Schilling, Magnetoconductance and photoresponse properties of disordered NbTiN films, *Physical Review B* **104**, 184514 (2021).
- [50] A. Semenov, B. Günther, U. Böttger, H.-W. Hübers, H. Bartolf, A. Engel, A. Schilling, K. Ilin, M. Siegel, R. Schneider, D. Gerthsen, and N. A. Gippius, Optical and transport properties of ultrathin NbN films and nanostructures, *Physical Review B* **80**, 054510 (2009).
- [51] A. Banerjee, R. M. Heath, D. Morozov, D. Hemakumara, U. Nasti, I. Thayne, and R. H. Hadfield, Optical properties of refractory metal based thin films, *Optical Materials Express* **8**, 2072 (2018).
- [52] L. Zhang, L. You, L. Ying, W. Peng, and Z. Wang, Characterization of surface oxidation layers on ultrathin NbTiN films, *Physica C: Superconductivity and its Applications* **545**, 1 (2018).
- [53] Y. P. Korneeva, D. Y. Vodolazov, A. V. Semenov, I. N. Florya, N. Simonov, E. Baeva, A. A. Korneev, G. N. Goltsman, and T. M. Klapwijk, Optical Single-Photon Detection in Micrometer-Scale NbN Bridges, *Physical Review Applied* **9**, 64037 (2018).
- [54] J. R. Clem and V. G. Kogan, Kinetic impedance and depairing in thin and narrow superconducting films, *Physical Review B* **86**, 174521 (2012).
- [55] K. Il'in, M. Siegel, A. Engel, H. Bartolf, A. Schilling, A. Semenov, and H. W. Huebers, Current-induced critical state in NbN thin-film structures, *Journal of Low Temperature Physics* **151**, 585 (2008).
- [56] K. Il'in, M. Siegel, A. Semenov, A. Engel, and H.-W. Hübers, Critical current of Nb and NbN thin-film structures: The cross-section dependence, *physica status solidi (c)* **2**, 1680 (2005).
- [57] H. Li, Y. Wang, L. You, H. Wang, H. Zhou, P. Hu, W. Zhang, X. Liu, X. Yang, L. Zhang, Z. Wang, and X. Xie, Supercontinuum single-photon detector using multilayer superconducting nanowires, *Photonics Research* **7**, 1425 (2019).
- [58] A. J. Kerman, E. A. Dauler, W. E. Keicher, J. K. Yang, K. K. Berggren, G. Gol'tsman, and B. Voronov, Kinetic-inductance-limited reset time of superconducting nanowire photon counters, *Applied Physics Letters* **88**, 2 (2006).
- [59] J. Pearl, Current distribution in superconducting films carrying quantized fluxoids, *Applied Physics Letters* **5**, 65 (1964).
- [60] H. Bartolf, *Fluctuation Mechanisms in Superconductors* (Springer Fachmedien Wiesbaden, Wiesbaden, 2016).
- [61] For a detailed derivation of Equations (1) and (2) see also the book of Tinkham [73, Eqs. (3.120), (3.137), and (6.67b)].
- [62] P. F. A. Alkemade and E. van Veldhoven, Deposition, Milling, and Etching with a Focused Helium Ion Beam, in *Nanofabrication*, edited by M. Stepanova and S. Dew (Springer Vienna, Vienna, 2012) pp. 275–300.
- [63] N. Li, M. S. Martin, O. Anderoglu, A. Misra, L. Shao, H. Wang, and X. Zhang, He ion irradiation damage in Al/Nb multilayers, *Journal of Applied Physics* **105**, 123522 (2009).
- [64] J. Shimizu, K. Yasuda, and C. Kinoshita, Formation process of defect clusters in copper and nickel under irradiation with helium ions, *Journal of Nuclear Materials* **212–215**, 207 (1994).
- [65] R. Behrisch and W. Eckstein, eds., *Sputtering by Particle Bombardment*, 1st ed., Topics in Applied Physics No. 110 (Springer Berlin Heidelberg, Berlin, Heidelberg, 2007).
- [66] Y. Ivry, C. S. Kim, A. E. Dane, D. De Fazio, A. N. McCaughan, K. A. Sunter, Q. Zhao, and K. K. Berggren, Universal scaling of the critical temperature for thin films near the superconducting-to-insulating transition, *Physical Review B* **90**, 214515 (2014).
- [67] I. Holzman and Y. Ivry, Superconducting Nanowires for Single-Photon Detection: Progress, Challenges, and Opportunities, *Advanced Quantum Technologies* **2**, 1800058 (2019).
- [68] D. B. Haviland, Y. Liu, and A. M. Goldman, Onset of superconductivity in the two-dimensional limit, *Physical Review Letters* **62**, 2180 (1989).
- [69] A. Bezryadin, C. N. Lau, and M. Tinkham, Quantum suppression of superconductivity in ultrathin nanowires, *Nature* **404**, 971 (2000).
- [70] A. Ruhtinas and I. J. Maasilta, Highly tunable NbTiN Josephson junctions fabricated with focused helium ion beam (2023), arxiv:2303.17348 [cond-mat].
- [71] S. P. Chockalingam, M. Chand, J. Jesudasan, V. Tripathi, and P. Raychaudhuri, Superconducting properties and Hall effect of epitaxial NbN thin films, *Physical Review B* **77**, 214503 (2008).
- [72] R. Radebaugh, Cryocoolers: The state of the art and recent developments, *Journal of Physics: Condensed Matter* **21**, 164219 (2009).
- [73] M. Tinkham, *Introduction to Superconductivity*, 2nd ed., Dover Books on Physics (Dover Publ, Mineola, NY, 2004).